aerospace

MDPI

Article

Coupling of Fluid and Particle-in-Cell Simulations of Ambipolar Plasma Thrusters

Willem van Lynden [1,*], Raoul Andriulli [1], Nabil Souhair [1,2], Fabrizio Ponti [1] and Mirko Magarotto [3]

[1] Alma Propulsion Laboratory, Department of Industrial Engineering (DIN), University of Bologna, 40126 Bologna, Italy; raoul.andriulli@unibo.it (R.A.); nabil.souhair2@unibo.it or nabil.souhair@uir.ac.ma (N.S.); fabrizio.ponti@unibo.it (F.P.)
[2] LERMA Laboratory, Aerospace and Automotive Engineering School, International University of Rabat, Rabat 11100, Morocco
[3] Department of Information Engineering (DEI), University of Padova, 35131 Padua, Italy; mirko.magarotto@unipd.it
* Correspondence: wvlynden@gmail.com

Abstract: Ambipolar plasma thrusters are an appealing technology due to multiple system-related advantages, including propellant flexibility and the absence of electrodes or neutralizer. Understanding the plasma generation and acceleration mechanisms is key to improving the performance and capabilities of these thrusters. However, the source and plume regions inside are often simulated separately, and no self-consistent strategy exists which can couple these different simulations together. This paper introduces the MUlti-regime Plasma Equilibrium Transport Solver (MUPETS), a self-consistent coupled model integrating a fluid solver for the plasma dynamics in the source, which are collision-driven, with a kinetic Particle-In-Cell (PIC) code for the plasma dynamics in the magnetic nozzle, which involve expansion across a diverging magnetic field. The methodology begins by solving the plasma source with the classical Bohm condition at the thruster's throat. The resulting plasma profiles (density, temperature, speed) are input into the PIC code for the magnetic nozzle. The PIC code calculates the plasma plume expansion and determines the electric field at the thruster's throat. This electric field is then used as a boundary condition in the fluid code, where it replaces the Bohm assumption, and the fluid simulation is repeated. This iterative process continues until convergence. In comparing the MUPETS results with those for an experimental thruster, the plasma densities at the thruster's throat differed by less than 2–5% between the fluid and PIC regions. The thrust predictions agreed with the experimental trend, and were kept well within the measurement's uncertainty band. These results validate the effectiveness of the coupling strategy for enhancing plasma thruster simulation accuracy.

Keywords: self-consistent simulation; ambipolar plasma thruster; fluid; particle-in-cell; magnetic nozzle

Citation: van Lynden, W.; Andriulli, R.; Souhair, N.; Ponti, F.; Magarotto, M. Coupling of Fluid and Particle-in-Cell Simulations of Ambipolar Plasma Thrusters. *Aerospace* **2024**, *11*, 880. https://doi.org/10.3390/aerospace11110880

Academic Editor: Martin Tajmar

Received: 29 September 2024
Revised: 21 October 2024
Accepted: 22 October 2024
Published: 25 October 2024

1. Introduction

Ambipolar Plasma Thrusters (APTs) represent a class of electric propulsion systems that create and accelerate a plasma using electromagnetic fields rather than electrodes. Among the most promising variants of APTs are Helicon Plasma Thrusters [1–6] (HPTs) and Electron Cyclotron Resonance Thrusters [7,8] (ECRTs). These devices generate plasma within a source chamber, where an antenna operating in the Radio Frequency (RF) or microwave range sustains the discharge. A magnetostatic field produced by electric or permanent magnets drives the power coupling of the RF waves into the plasma [9], enhances plasma confinement, and boosts propulsive performance via the magnetic nozzle effect [10,11]. APTs offer multiple system-level advantages, including propellant flexibility, simpler design, and longer lifetimes, thanks to their omission of any anodes and cathodes.

These advantages make them highly appealing for applications in the SmallSat market [12], interplanetary missions [13], and Air-Breathing Electric Propulsion (ABEP) missions [14,15].

Despite their potential, the performance of APTs has not yet fulfilled their promise, as current thrusters are marked by only moderate propulsive efficiencies. For instance, the efficiency of HPTs has not yet exceeded 30% [16]. To enhance the performance of APTs, a deeper understanding of the plasma generation and acceleration mechanisms is required. To this end, numerous modeling efforts [17–19] have sought to accurately predict the operational behaviors and theoretical limits of these thrusters. However, this is a challenging effort due to the existence of different flow regimes in different sections of the thruster. Within the plasma source, the flow behaves as a continuum governed by the propagation of electromagnetic waves, plasma transport, and their mutual coupling. Downstream in the expanding plume of the magnetic nozzle region, the plasma density drops sharply and the main phenomena at play become the acceleration and magnetic detachment of the plasma.

Codes that describe the plasma state in the source chamber are most often fluidic [20–22], assuming that the many collisions inside the high-density source [2] lead to thermal equilibrium and Maxwellian velocity distribution functions [23]. Meanwhile, for description of the plasma plume in the magnetic nozzle, where far fewer or even no collisions take place, a kinetic approach is favored, often in the form of Particle-in-Cell (PIC) simulations [24,25]. PIC codes, which group the plasma particles into macroparticles and then solve the motion of these particles individually, are marked by high computational cost compared to fluid codes. This computational cost increases with the plasma density; consequently, few models employ PIC for the high-density source chamber.

Thus, numerical APT studies can either treat each region with different solvers appropriate to each, or use a hybrid model [26,27] across the entire thruster. Simulating the source and plume separately has the advantage of codes that can be more specific in handling the peculiar phenomena of each region [28–30]. Simulating the regions as one with a hybrid model that selectively uses fluid or kinetic methods for different plasma particles has the advantage of simulating the full thruster with one model and simulating the transition between sections; however, it provides a less specific approach in each region. On the other hand, when using a specialized solver for each section [17,22,28], the transition and required interfacing between the two regions presents a challenge for simulating the full thruster. For example, problems in continuity between separated models can occur across the flow regime transition [28]. Instead, approaches often focus on a single region [31] and handle the other region through a global model [19], although this reduces the accuracy of the overall solution. As of yet, no self-consistent strategy exists for coupling different simulations of source and plume together.

This work proposes an innovative self-consistent methodology for coupling a fluid solver [20] to handle the plasma source region and a Particle-In-Cell (PIC) code [25] dedicated to the magnetic nozzle region. This methodology is compared against established numerical approaches and validated through experimental data [28]. By self-consistently coupling the plasma state across flow regimes, the proposed approach aims to improve the ability to predict propulsive performance by treating each regime using a specialized solver. Within the scope of the present paper, this strategy is exploited for modeling APTs; however, it could also be useful for improving the modeling of broader plasma applications, such as other electric propulsion systems or material etching tasks [32,33].

2. Methodology

The model coupling methodology is based on a 2D-3V axisymmetric representation of an APT design, shown in Figure 1. The coupled model simulates the plasma source section and the free space outside of the thruster, where a diverging magnetic field forms the magnetic nozzle, thereby still forming part of the propulsive system. A constant propellant mass flow of neutral gas is injected at the back-wall. Figure 1 also shows the fluid and PIC domains; the fluid domain encompasses the entire source chamber, extending radially

from the thruster's centerline to the chamber walls and axially from the back-wall to the outlet. The plasma plume expanding into free space is modeled as a kinetic flow, and as such is covered by the kinetic PIC domain. The transition between these domains occurs at the throat of the thruster (at $z = z_{throat}$), consistent with approaches where the regions are treated separately [17,28].

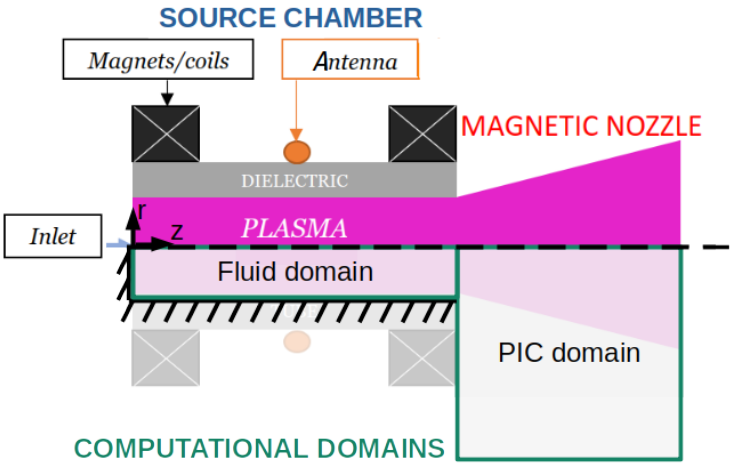

Figure 1. Model of the APT geometry, showing the locations of the source chamber and magnetic nozzle along with the assumed locations of the fluid and kinetic regimes.

2.1. Models

The coupling methodology focuses on the steady-state conditions achieved by the fluid and kinetic models. Both of these models consider the following plasma species: neutrals, singly-charged positive ions, and electrons. The fluid model separates the neutrals further into neutrals in the ground state and neutrals in multiple excited states [21], while in the kinetic model the excited species are assumed to immediately decay to the ground state

The fluid model governs plasma dynamics using three fundamental equations: conservation of mass for each species, conservation of energy, and the Poisson equation for plasma potential (ϕ). In this paper, the methodology is presented only for a Drift Diffusion [34] (DD) implementation; however, generalization to fluid models based on the solution of the full momentum equations is straightforward. The use of the DD formulation for the transport equations of each plasma species is justified if its collision frequency is higher than the estimated velocity gradient [35]. For typical discharges applied on HPTs, this condition is respected if the neutral pressure is above 1 mTorr [36].

The kinetic model tracks plasma species macroparticles, solves their motion under electromagnetic forces, and uses the Poisson equation for ϕ. The fluid and kinetic models are further expanded upon in Appendix A.

2.2. Coupling

The coupling scheme is shown in Figure 2. The scheme is iterative, running h parent iterations until convergence. For each iteration h, the fluid solver runs until achieving the steady state. The fluid plasma properties at the throat are then used as input to the kinetic solver, which also runs until achieving the steady state. The kinetic results then are used to correct the initial throat BCs of the fluid simulation, after which a new parent iteration $h + 1$ starts. Initially ($h = 0$), the plasma source is solved assuming the classical Bohm condition at the throat. For subsequent parent iterations ($h + 1$), the fluid model uses the corrected BCs, replacing the Bohm condition with the kinetic potential gradient to ensure self-consistent coupling. Convergence is achieved when the axial electron density profiles between iterations differ by less than 10%, which is the uncertainty in measuring the electron current density [37,38].

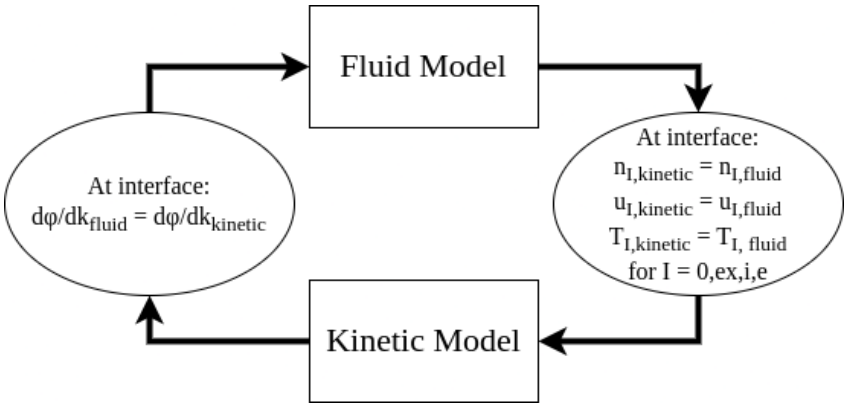

Figure 2. Solver scheme.

Coupling Interface Boundary Conditions

Figure 3 shows the applied BCs for the thruster domain. This section describes the BCs used at the interface between the two models, i.e., the throat. The rest of the BCs used in each model are further described in Appendix A.

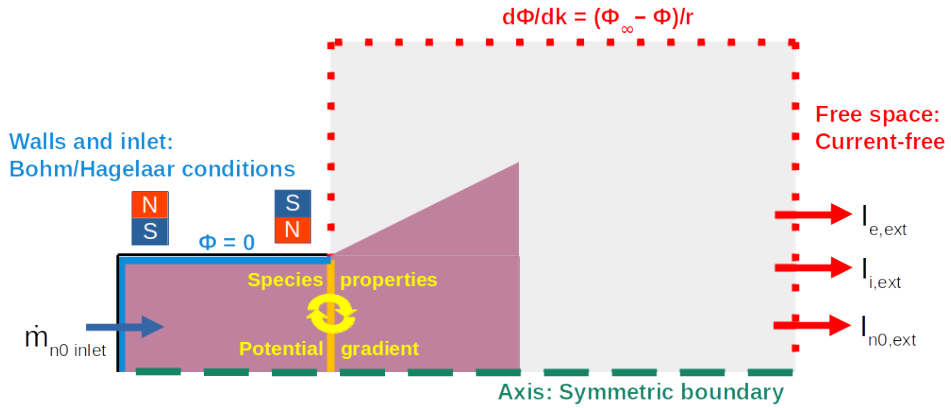

Figure 3. Boundary conditions applied on the axisymmetrical thruster domain.

At the interface, the fluid model assumes a developed flow for ions and neutrals, whie the BC, with $\hat{k}$ being the unit vector normal to the throat surface, is provided by

$$\left.\frac{dn_{i,0,ex}}{d\hat{k}}\right|_{Fluid} = 0. \tag{1}$$

For the initial fluid simulation at $h = 0$, Poisson's equation is solved by imposing a zero-current condition across the outlet:

$$\Gamma_{e_{\hat{k}}}|_{Fluid} = \Gamma_{i_{\hat{k}}}|_{Fluid}. \tag{2}$$

Rewriting Γ_e in its drift-diffusion formulation [20] and substituting the electric field E with $-\nabla\phi$ provides the initial plasma potential BC for $h = 0$:

$$\left.\frac{d\phi}{d\hat{k}}\right|_{Fluid,h=0} = \frac{\Gamma_{i_{\hat{k}}} + D_e\frac{dn_e}{d\hat{k}}}{n_e\mu_e}. \tag{3}$$

For $h = 0$, a BC is still required for the behavior of the electrons. To ensure the stability of the fluid solver, the electron flux is modeled as Equation (4); the Bohm sheath criterion [39] is used by enforcing the equality of fluxes ($\Gamma_e = \Gamma_i$) and quasi-neutrality. This approach has

been proven to be stable for bootstrapping the simulation in a stable manner, as reported in [20,40,41], and is corrected in subsequent iterations $h+1$.

$$\Gamma_{e_{\hat{k}}}\big|_{Fluid,h=0} = v_B n_e \tag{4}$$

Finally, the electron energy density follows the electron density flux [20]:

$$\Gamma_{\varepsilon_{\hat{k}}}\big|_{Fluid} = \frac{2}{3}\left(\frac{1}{2}\left(1+\ln\left(\frac{m_i}{2\pi m_e}\right)\right)+2\right)\cdot\Gamma_{e_{\hat{k}}}\Big|_{Fluid}. \tag{5}$$

For subsequent iterations $h+1$, the plasma potential BC is corrected by the kinetic simulation results of h:

$$\frac{d\phi}{d\hat{k}}\bigg|_{h+1,Fluid} = \frac{d\phi}{d\hat{k}}\bigg|_{h,PIC}. \tag{6}$$

The earlier assumed zero-current condition provided by Equation (2) are now directly applied to the electron density for $h+1$. Thus, in all iterations where $h>0$, the assumption of the Bohm condition at the throat is removed, allowing the electron outflow to evolve self-consistently.

In summary, the coupling of the fluid model's BCs to the kinetic model is achieved by obtaining the kinetic potential gradient and assuming steady-state operation. Only the interface BCs for the potential (ϕ) and electron density (n_e) are updated. Instead of being predetermined by the Bohm speed, the particle speed at the interface is computed self-consistently, with the ion flux driven by the previous iteration's electric field and the electrons' response determined under the current-free assumption.

The kinetic model requires the number density, velocity, and temperature (n_I,v_I,T_I) of the plasma species at the throat in order to construct the sampling distribution function for each particle species (PDF) [29] and velocity distribution function for the PIC solver (VDF). Macroparticles are sampled from the PDF and VDF, and are injected into the numerical kinetic domain from the interface. To maintain a current-free global plasma flow as determined by the steady-state operation of an ambipolar plasma thruster [25,42], the kinetic model balances the injected electron flux against the total outgoing charge of species leaving the kinetic domain through the free-space boundary. More details on this balance are provided in Appendix A. Considering the boundary condition on the potential field, a Dirichlet (i.e., $\phi_b = 0\,V$) condition is imposed. This can be performed as in the kinetic routine calculation, with the potential included only as a derivative; hence, any constant offset will not affect the results. The potential field offset is then taken into account during postprocessing.

2.3. MUPETS

The coupling strategy is implemented in the MUlti-regime Plasma Equilibrium Transport Solver (MUPETS), a Python code developed at the Alma Propulsion Laboratory of the University of Bologna in cooperation with the University of Padova. MUPETS manages the fluid and kinetic solvers as well as the coupling methodology. The fluid model uses the plasmaFoam solver [40,43], based on the OpenFOAM framework [44] and derived from the 3D-VIRTUS code [41], while the kinetic model uses an adapted version [29] of the Starfish PIC code [45]. Further details on the plasmaFoam and Starfish codes are provided in Appendix B. The modularity of MUPETS allows for easy replacement or updating of solvers; thus, the proposed coupling methodology can be used together with a range of different solvers, allowing for the choice of a solver that best suits the thruster design and operating conditions. MUPETS responsibilities include:

1. Preprocessing simulation cases:
   - For fluid, $h=0$: Setting up the initial case with starting values.
   - For fluid, $h>0$: Updating case with BC values from kinetic simulation.
   - For kinetic, h: Constructing PDFs and VDFS for macroparticles.

2. Running simulations with relevant solvers and parameters.
3. Postprocessing the converged solutions into a common data structure.
4. Adjusting conditions for the next simulation based on the current solutions.
5. Loop control until the convergence criteria are met.
6. Handling numerical domain division.

2.4. Propulsive Performance

The performance of a thruster can be measured by its thrust level, specific impulse, power consumption, and associated efficiencies. The thrust can be calculated during postprocessing of the combined fluid–kinetic data of the entire thruster domain. After this, the other metrics can be derived from the thrust and other postprocessed metrics or input variables, such as the injected propellant mass flow and input power. The thrust is taken to be the momentum flux of the plasma jet [46]:

$$F = \sum_{I=i,e,0} \int_A (p_I + m_I n_I u_{Iz}^2) dA. \tag{7}$$

Several assumptions stemming from the coupled model simplify the thrust calculation. First, the heavy particles are considered 'cold', with $T_e >> T_i, T_0$, allowing the pressure terms for heavy species to be neglected. The electron momentum term is also neglected due to $m_e << m_i, m_0$. The thrust contribution from neutrals is assumed to be negligible due to their lower velocity [47] and temperature [48]. Additionally, momentum losses to the wall are considered negligible [46] due to magnetic shielding [10,19,49] of the source chamber walls. The momentum flux then simplifies to the sum of the pressure force from the source chamber and the momentum force enhanced by the magnetic nozzle [46]:

$$F_{cham} \approx (1 + C^2)\pi R_*^2 n_{e*} q T_{e*} \tag{8}$$

$$F_{mag} = \int_V J_\theta B_r dV \tag{9}$$

$$F_{thrust} = F_{cham} + F_{mag} \tag{10}$$

where F_{cham} represents the thrust from the source chamber due to static electron pressure against the back plate inside the source, shown in Figure 4. It is approximated using the average electron density n_{e*} and temperature T_{e*} at the outlet [19], with R_* being the outlet radius and C the ratio of the ion drift velocity to the Bohm velocity. F_{mag} represents the magnetic thrust, calculated as the volume integral of the Lorentz force due to the radial magnetic field B_r and the azimuthal current, shown as F_z in Figure 4.

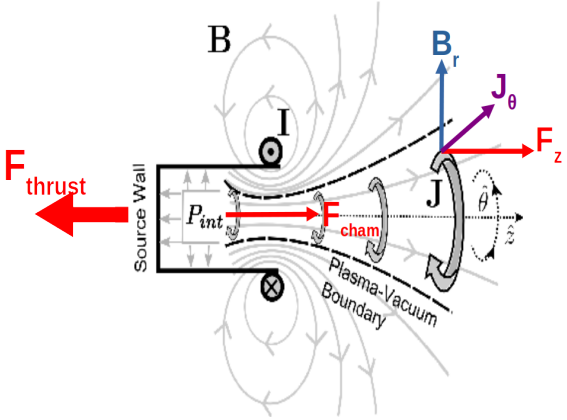

Figure 4. The thrust imparted by the plasma exhaust [50] (F_{thrust}) consists of F_{cham} and the volume integral of the axial Lorentz force component (F_z) in the magnetic nozzle; B is the magnetic field strength, and J is the azimuthal current of the charged particles.

3. Experiment

Through a numerical study, we aimed to determine whether the presented coupling methodology results in improved accuracy by comparing experimental thrust measurements with numerical thrust predictions from MUPETS and other numerical approaches [28] for a laboratory thruster [3]. Thus, in this study we focus on predicting and comparing the thruster plasma state of the resulting thrust against experiments; convergence studies of the MUPETS code have been presented in an earlier work [51].

3.1. Experimental Thruster

The laboratory RF ambipolar thruster developed by the University of Padova [52–54] features a source chamber with radius and length of 7 mm and 60 mm, respectively. Neutral Xenon atoms are injected into the thruster at the inlet at a constant mass flow rate of 150 µg s^{-1}. The magnetic field is generated by two sets of permanent magnets arranged in opposing directions. Thrust measurements were taken at six power settings ranging from 23 W to 69 W.

3.2. Numerical Simulations

The thruster geometry was maintained as described for the experimental thruster in Section 3.1. The minimum cell size in the fluid domain was set to 50 µm, while that of the kinetic domain was set to 500 µm. The mesh is shown in Figure 5. Further details on the mesh and run parameters of each code can be found in Appendix B. The magnetic field created by the permanent magnets was modeled separately and provided to OpenFOAM and Starfish for the source chamber and expanding magnetic nozzle section, respectively. The orientation of the magnets and the resulting geometry are shown in Figure 6a. Collisions in the rarefied plume were included for increased fidelity, with collision rates and chemistry coefficients for the Xenon propellant sourced from the literature [21,43,55–61]. The RF coupled power P_w was simulated at points spaced 15 W apart, ranging from 15 W to 57 W. The 57 W point was used instead of 60 W for better comparison with previous simulations of this thruster. The space surrounding the thruster was modeled as a vacuum.

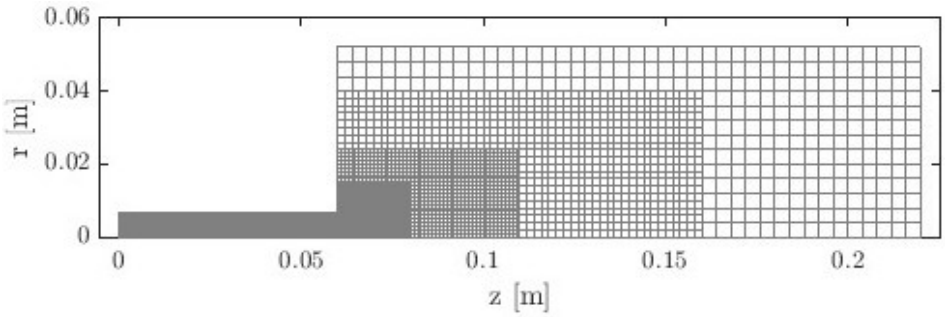

Figure 5. MUPETS combined mesh.

The hardware used to run MUPETS consisted of four Intel(R) i7-7700 Cores(TM) @ 3.60 GHz and 64 Gb of RAM, which resulted in a convergence time of 2–3 weeks. The majority of this time was consumed by running the PIC code. A PIC code optimized to reduce this time is currently under development.

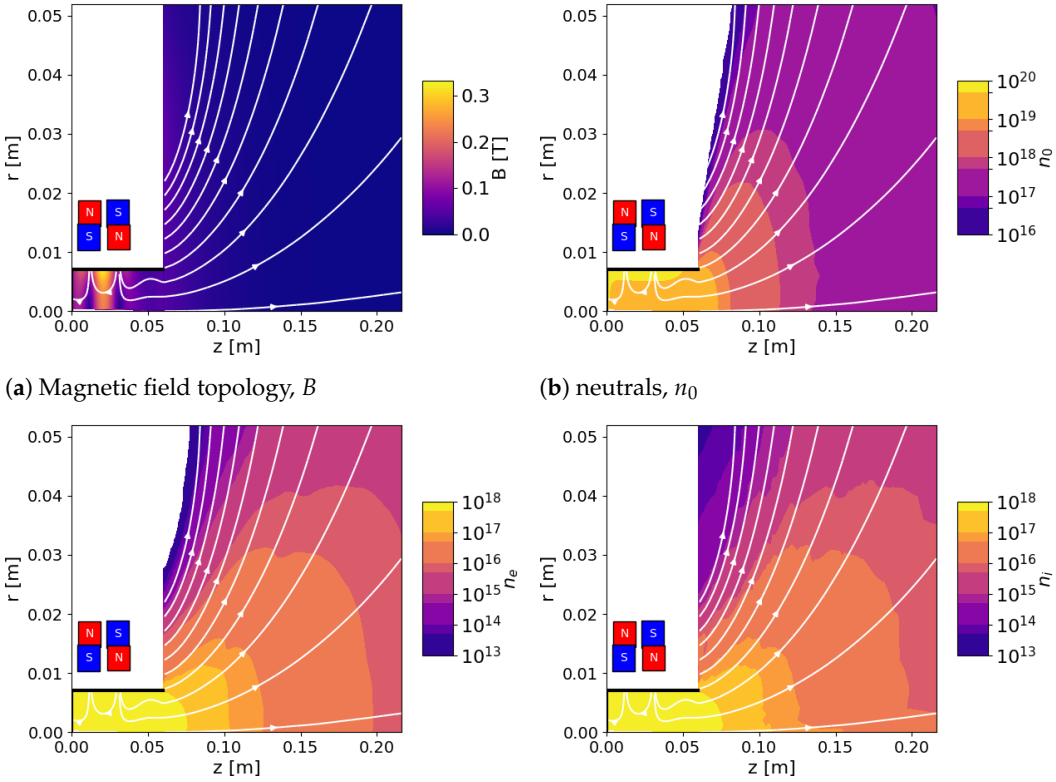

(**a**) Magnetic field topology, B

(**b**) neutrals, n_0

(**c**) electrons, n_e

(**d**) ions, n_i

Figure 6. Magnetic field B and species density n_0, n_e, n_i on the full thruster z-r domain of MUPETS (57 W).

4. Results and Discussion

4.1. Plasma Profiles

The full thruster 2D profiles of the magnetic field and plasma at 57 W solved by the coupled model are shown in Figure 6. Additionally, the species density profiles zoomed in at the source chamber are presented in Figure 7. The interaction of the expansion plumes with the magnetic field is evident in the plume region near and slightly outside of the outlet (Figure 6b–d). The magnetized electrons expand along the magnetic field lines, while the non-magnetized ions, driven by the resulting electric field, follow the electrons closely along the magnetic field lines [49]. Meanwhile, the neutral particles, lacking any charge, are unaffected by the magnetic field and expand into free space. Inside the source (Figure 7), the electrons also follow the magnetic field topology closely. The magnetic cusp regions show enhanced plasma transport to the walls [4], causing increased local plasma losses. The neutral density increases near the walls, showing that plasma recombination into neutrals at the walls dominates the neutral chemistry in this region, which is in agreement with other model and experiment findings [39]. In the bulk of the plasma near the axial center line, ionization dominates and the neutral density decreases. The peak neutral density is located at the magnetic cusp impingement sites on the wall, where the neutral density increases to a few percentage points above its original injected density through recombination, confirming the increased local plasma loss areas. The source results are qualitatively consistent with measurements performed on helicon plasma sources [62,63].

The area-averaged profiles of the charged species densities are shown in Figure 8, demonstrating near-continuity across the regime transition along the thruster's axial length. At the outlet, which separates the fluid and kinetic domains, discontinuities between the models in predicted ion and electron densities are kept below 2–5%.

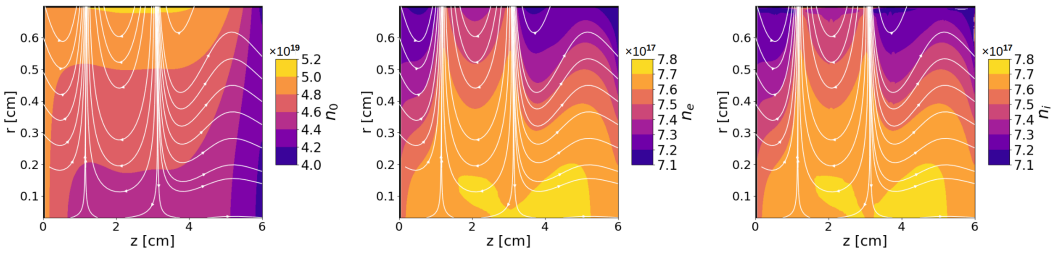

(**a**) neutrals (n_0) in the source (**b**) electrons (n_e) in the source (**c**) ions (n_i) in the source

Figure 7. Species density n_0, n_e, n_i on the source z-r domain of MUPETS (57 W).

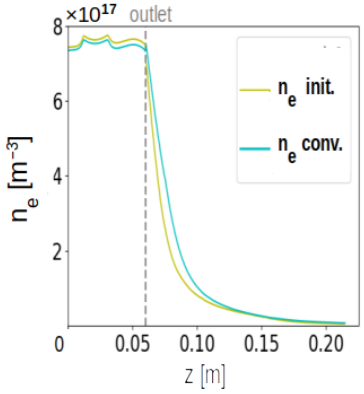

Figure 8. Initial and converged area-averaged plasma electron density n_e along the thruster's axial length.

4.2. Thrust Predictions

The predicted thrust from MUPETS at various power levels is reported in Table 1, together with the specific impulse and thrust efficiency obtained through $I_{sp} = \frac{T}{g_0 \dot{m}}$ and $\eta = \frac{T^2}{2\dot{m}P_{in}}$, respectively. The table also includes the error of the prediction with respect to the experimental trend, calculated as follows:

$$Error = \frac{|T_{sim} - T_{exp,trend}|}{T_{exp,trend}} \cdot 100\%. \tag{11}$$

The thrust is seen to increase almost linearly with the power, consistent with ionization ratios below 10% [29]. The measured propulsive performance across the tested low-power ($Pw \lesssim 100$ W) range is in line with that of commercial low-power RF APTs [13,64]. The thrust predictions were compared to the experimental measurements [3] in Figure 9. Initially, MUPETS underpredicts the thrust, similar to earlier separated approaches [65]. However, iterative corrections to the plasma flow through the thruster yield increased thrust, aligning more closely with the experimental trends. Overall, MUPETS demonstrates self-corrective behavior at all power levels. It occasionally overshoots the experimental trendline (57 W) at high power levels, while at lower power levels it exhibits a more steady but slow incremental increase towards the experimental fit (15 W). The coupling strategy appears to work best for the middle-power range, as for the simulations at 30 W and 45 W the initial large errors (≈50%) in thrust prediction are reduced to just 0.3% and 6%, respectively.

Table 1. Propulsive performance metrics.

Power [W]	Thrust [mN]	Error [%]	I_{sp} [s]	η [%]
15	0.17	20	117	0.7
30	0.45	0.3	308	2.3
45	0.64	6	436	3.1
57	1.01	16	689	6.0

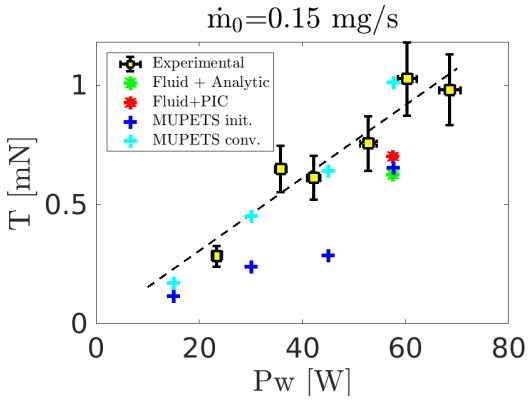

Figure 9. MUPETS numerically-predicted thrust (T) compared against experiments [3] and earlier simulations [65] across coupled power (Pw); here, "init." refers to the initial prediction of MUPETS, while "conv." refers to the converged prediction.

4.3. Convergence

To showcase the convergence of the iterative loop, the differences between iterations in the cross-sectional averaged electron densities are plotted along the axial direction in Figure 10, together with the maximum difference after each iteration. Here, the difference is calculated as follows:

$$diff = \frac{\int n_e(z,r)^h r dr}{\int r dr} - \frac{\int n_e(z,r)^{h-1} r dr}{\int r dr}. \quad (12)$$

The process converges rapidly; after the second iteration, the electron density profile already differs less than 10% everywhere along the thruster's longitudinal axis, meeting the convergence criteria set out in Section 2.2. The largest differences exist in the kinetic plume.

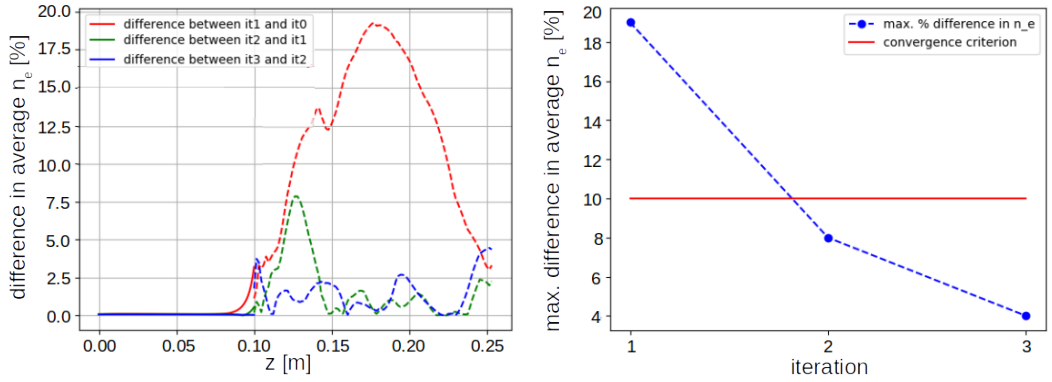

(**a**) (**b**)

Figure 10. Convergence plots for 15 W: (**a**) relative differences of the axial average n_e profiles between iterations and (**b**) convergence of maximum n_e difference after each iteration.

5. Conclusions

A self-consistent coupling method between fluid and Particle-In-Cell (PIC) solvers has been developed and integrated into a multi-regime plasma model, namely, the MUlti-regime Plasma Equilibrium Transport Solver (MUPETS), to simulate plasma transport and propulsion performance in an Ambipolar Plasma Thruster (APT). MUPETS controls two distinct plasma transport models: a fluid model based on the plasmaFoam code [40,43], and a kinetic model based on the Starfish code [29,45], running them iteratively to self-consistently solve the full thruster domain that includes both the fluid and kinetic regions. Information exchange between the models at the regime boundary ensures continuity,

with the fluid model providing plasma species densities, velocities, and temperature to the kinetic model and the kinetic model supplying the electric field to the fluid model.

The MUPETS coupling strategy shows significant accuracy when validated against experimental thrust data, with discontinuities in the predicted ion and electron densities at the outlet separating the fluid and kinetic domains minimized to 2–5%. The prediction error fell between 0.3% and 20% for the tested Xenon-fed laboratory thruster [3] operating between 15 W and 57 W, which is well within the measurement's uncertainty band.

The MUPETS code and its coupling methodology present improved predictions of a thruster's propulsive performance without the need for the high computational cost incurred by simulating the source chamber region through PIC. The proposed methodology is applicable for further studies in electric propulsion and other plasma applications involving multiple regimes. It imposes no additional assumptions on plasma properties at the coupling interface beyond current-free flow; in addition, its relevance extends to various solvers, making it adaptable to numerous cases and codes beyond those considered in this study.

Author Contributions: Conceptualization: W.v.L. and N.S.; methodology: W.v.L., N.S, R.A., and M.M.; software: W.v.L., N.S., R.A., and M.M.; validation: W.v.L. and M.M.; formal analysis: W.v.L., N.S., R.A., and M.M.; investigation: W.v.L.; resources: W.v.L.; data curation: W.v.L.; writing—original draft preparation: W.v.L.; writing—review and editing: N.S., R.A., M.M., and F.P.; visualization: W.v.L.; supervision: N.S., R.A., M.M., and F.P.; project administration: W.v.L.; funding acquisition: F.P. All authors have read and agreed to the published version of the manuscript.

Funding: This work has been developed within the BOOST (Building blOcks for iOdine thruSTers) project, a research initiative funded by the European Union. The authors acknowledge the corresponding financial support of the Horizon Europe programme under GA 101135216.

Data Availability Statement: The raw data supporting the conclusions of this article will be made available by the authors on request.

Conflicts of Interest: The authors declare no conflicts of interest.

Nomenclature

The following abbreviations are used in this manuscript:

Abbreviation	**Definition**
APT	Ambipolar Plasma Thruster
BC	Boundary Condition
DD	Drift Diffusion
ECRT	Electron Cyclotron Resonance Thruster
EP	Electric Propulsion
HPT	Helicon Plasma Thruster
MUPETS	MUlti-regime Plasma Equilibrium Transport Solver
PDF	Particle Distribution Function
RF	Radio Frequency
VDF	Velocity Distribution Function

Symbol	**Definition**	**Unit**
B	Magnetic field	[T]
C	Ion drift-to-Bohm velocity ratio, capacitance	[-]
D	Diffusion coefficient	$[m^2s^{-1}]$
E	Electric field	$[Vm^{-1}]$
F	Force	[N]
f	Mass factor	[-]
h	Model iteration	[-]
g_0	Gravitational standard at Earth	$[ms^{-2}]$
I_{sp}	Specific impulse	[s]
J	Current	$[Cm^{-2}s]$
k_B	Boltzmann constant	$[m^2kgs^{-2}K^{-1}]$

m	Mass	[kg]
$\dot{m}$	Mass flow rate	[kgs^{-1}]
n	Number density	[m^{-3}]
p	Pressure	[Nm^{-2}]
P	Power	[W]
q	Particle charge	[C]
R_*	Source chamber radius	[m]
r	Radial direction	[m]
T	Thrust, Temperature	[N], [K]
v	Velocity	[ms^{-1}]
V	Volume	[m^3]
z	Axial direction	[m]
k	Normal direction to a surface	[-]
Γ	Particle flux	[$m^{-2}s^{-1}$]
γ	Scaling factor	[-]
ϵ_0	Permittivity of free space	[$m^{-3}kg^{-1}s^4$ A^2]
η	Thrust efficiency	[-]
λ_D	Debye length	[m]
μ	Mobility coefficient	[$m^2V^{-1}S^{-1}$]
π	Pi	[-]
ϕ	Plasma potential	[V]
ω_{pe}	Plasma frequency	[$rads^{-1}$]

Subscript	**Definition**
I	General species
0	Neutral ground state
ex	Neutral excited state
e	Electron
i	Ion
k	Normal to surface
r	Radial direction
θ	Azimuthal direction
*	At throat
∞	At free space
inlet	At inlet boundary
wall	At wall boundary
ext	External boundary
fluid	Of fluid model or code
kinetic, PIC	Of kinetic model or PIC code
h	Coupled model iteration
n	Kinetic model iteration
I	General species

Appendix A. Physical Models

Appendix A.1. Fluid Model

The fluid model separately considers the neutral atoms, excited atoms in the lumped 1Sr, 1Sm, and 2P states [21], single positive ions, and negative electrons. These species are denoted with the subscripts 0, $1Sr$, $1Sm$, $2P$, i, and e, respectively. The plasma dynamics in the fluid model are governed by a set of three fundamental equations: the conservation of mass, the conservation of energy, and the Poisson equation, shown respectively in Equations (A1)–(A3). Equation (A1) is considered for each species number density n_I, where the subscript I denotes the species, whereas Equation (A2) only considers the electron energy density n_ε, as the energy density of the other species is negligibly small [40,43,65]. Equation (A3) complements the conservation equations by solving the plasma potential ϕ, obtaining the internal electric field and completing the model's governing equations.

$$\frac{dn_I}{dt} + \nabla \cdot \vec{\Gamma}_I = R^I_{chem} \tag{A1}$$

$$\frac{dn_\varepsilon}{dt} + \nabla \cdot \vec{\Gamma}_\varepsilon - \nabla\phi \cdot \vec{\Gamma}_e = Pw - P_{chem} \tag{A2}$$

$$\nabla^2\phi = -q\left(\frac{n_i - n_e}{\varepsilon_0}\right) \tag{A3}$$

In Equations (A1) and (A2), R^I_{chem}, Pw, and P_{chem} are respectively the source or sink term for the species plasma reactions, the power coupled to the plasma, and the power lost or gained through plasma reactions. The species density flux Γ_I is modeled through the DD approximation [34] shown in Equation (A4):

$$\vec{\Gamma}_I = -D_I \nabla n_I \pm \mu_I \vec{E} \cdot n_I \tag{A4}$$

where D_I and μ_I are the diffusion and mobility of the species, respectively, while E is the electric field. The magnetized electron diffusion and mobility shall be tensors [66], while the diffusion and mobility of the heavy species shall be scalar coefficients [20]. The sign in $\pm$ follows the charge of the species. Finally, in Equation (A3), q is the electric charge and ε_0 is the permittivity of the free space. The coefficients D_I and μ_I and terms R^I_{chem}, Pw, and P_{chem} are expanded upon in [20].

Conventional boundary conditions (BCs) are set for the source inlet and walls of the fluid model, while the outlet is treated separately in order to couple it to the kinetic model. Considering Poisson's equation first, both the inlet and walls are assumed to be grounded, and consequently have zero potential [20]:

$$\phi_{inlet,wall} = 0. \tag{A5}$$

For conservation of mass, the BCs imposed on the impinging fluxes $\Gamma_{I_{\hat{k}}}$ at the inlet and wall (with $\hat{k}$ being the normal direction to the inlet or wall) are treated differently for the different species. The following three groups are considered: light electrons, heavy neutrals in the ground state, and heavy ions and excited neutrals. The light electron transport at the inlet and walls is modeled through the Bohm sheath criterion [39]. This criterion imposes the Bohm velocity [67], $v_B = \sqrt{\frac{qTe}{m_i}}$ upon the electrons, as shown in Equation (A6).

$$\Gamma_{e_{\hat{k},inlet,wall}} = v_B n_e \tag{A6}$$

The electron energy density is linked to the electron density and temperature following $n_\varepsilon = \frac{3}{2} n_e T_e$ [68]. The BC for the plasma's energy flux is then determined from the Bohm sheath criterion [21,69], as shown in Equation (A7):

$$\Gamma_{\varepsilon_{\hat{k},inlet,wall}} = \frac{2}{3}\left(\frac{1}{2}\left(1 + \ln\left(\frac{m_i}{2\pi m_e}\right)\right) + 2\right) \cdot \Gamma_{e_{\hat{k},inlet,wall}}. \tag{A7}$$

The heavy ions and excited neutrals are modeled through the Hagelaar conditions [70]. The BC for single positively-charged ions [20] is provided by Equation (A8)

$$\Gamma_{i_{\hat{k},inlet,wall}} = \mu_i E_{\hat{k}} + \frac{1}{2} n_i v_{th_i}. \tag{A8}$$

For the excited chargeless neutrals ($I = 1Sr, 1Sm, 2P = ex$), the electromagnetic diffusion component drops out and the BC becomes Equation (A9)

$$\Gamma_{ex_{\hat{k},inlet,wall}} = \frac{1}{2} n_{ex} v_{th_{ex}}. \tag{A9}$$

At the wall and inlet, neutrals in the ground state are gained through recombination of impinging ions and electrons as well as from excited neutrals falling back to their ground state [20]. The ground state neutral flux at the wall $\Gamma_{0_{wall}}$ equals the negative sum of the impinging ion flux and excited neutral flux, as shown in Equation (A10). The BC at the source inlet includes an additional term representing the injected mass flow of neutral propellant gas [20], as shown in Equation (A11).

$$\Gamma_{0_{\hat{k},wall}} = -\Sigma_{j=i,ex}\Gamma_{j_{\hat{k},wall}} \tag{A10}$$

$$\Gamma_{0_{\hat{k},inlet}} = -\Sigma_{j=i,ex}\Gamma_{j_{\hat{k},inlet}} - \frac{\dot{m}}{A_{inlet}M_0} \tag{A11}$$

The injected propellant mass flow, the inlet boundary surface area, and the molecular mass of the neutral particles are denoted by $\dot{m}$, A_{inlet}, and M_0 respectively.

Appendix A.2. Kinetic Model

The kinetic model tracks different macroparticles representing the different species (positive ions, negative electrons, and neutrals). For the neutral macroparticle group, the excited and ground state neutrals are grouped together. The model's governing equations consist of Equation (A12) to solve the motion of each macroparticle via Boris' algorithm [71] and again Poisson's equation Equation (A3) to solve the plasma potential ϕ.

$$\frac{\mathrm{d}\vec{v_p}}{\mathrm{d}t} = \frac{q_p}{m_p}\left(\vec{E} + \vec{v_p} \times \vec{B}\right) \tag{A12}$$

The kinetic regime exists outside of the physical thruster structure and extends into the infinite free space outside of it. Taking r as the total distance from the center of the thruster, the model requires an external domain boundary limit [42] with a set of BCs that model this free space, where $r \to \infty$ to constrain the model's domain. In free space, the potential is assumed to behave as $\phi \approx 1/r$ [25], causing the gradient across the external boundary to be modeled as Equation (A13), as shown in Figure 3, where ϕ_∞ is the potential at an infinite distance from the thruster outlet and $\hat{k}$ is the direction normal to the external boundary.

$$\frac{\mathrm{d}\phi}{\mathrm{d}\hat{k}} = \frac{1}{r}(\phi_\infty - \phi) \tag{A13}$$

Ions and electrons are removed from the simulation domain when reaching the casing and thruster outlet [42], representing recombination or backflow into the source. When the charged species reach the external boundaries, the ions are also removed [42], while the electrons are treated differently. At steady state, the plasma plume exhausted by an ambipolar plasma thruster must be globally current-free, characterized by

$$J_{i-,ext} + J_{e,ext} = -\sum_{i+} J_{i+,ext}, \tag{A14}$$

where $J_{i-,ext}$ and $J_{e,ext}$ denote the current across the external free space boundary due to negative ions and electrons, respectively, while $J_{i+,ext}$ denotes the current due to any ions with single, double, or higher positive charge.

To maintain this, an energy-based criterion [25] is used to determine whether the electrons escape the potential drop over the plume or become trapped inside of it. First, the total energy of electrons is calculated in Equation (A15).

$$E_{tot} = \frac{1}{2}m_e v^2 - q_e\phi \tag{A15}$$

If $|E_{tot}| > |q\phi_\infty|$, then the electrons will escape the plume and be removed from the simulation domain; if $|E_{tot}| \leq |q\phi_\infty|$, then they become trapped, and their velocity is

mirrored ($\vec{v} = -\vec{v}$). To reflect enough electrons to maintain a global current-free plasma [42], the value of ϕ_∞ is controlled in the PIC iterations by a virtual free-space capacitance C through

$$\phi_\infty^{n+1} = \phi_\infty^n + \frac{1}{C}\left(J_{i,ext}^n + J_{e,ext}^n\right)\Delta t. \tag{A16}$$

Before a global current-free plasma outflow is achieved at steady state, any nonzero net current leaving the open boundaries during the transient must be reinjected into the domain via the thruster outlet in order to complete the circuit. The injected electron current J_{e*} must also be controlled such that the quasi-neutrality condition holds at the source outlet. The ions are injected with a constant current $J_{i*} = \pi R_*^2 q n_{i*} v_{i*}$, where n_{i*} and v_{i*} are obtained from the fluid model. Instead, the injected electron current is updated each time step according to

$$J_{e*}^{n+1} = \left(J_{i,ext}^n + J_{e,ext}^n\right) + \frac{n_{i0}^n}{n_{e0}^n} J_{e*}^n, \tag{A17}$$

where n_{i0} and n_{e0} are the ion and electron densities at the thruster outlet as solved by the PIC model instead of the fluid model. For further details on the formulation of this PIC model as well as derivation, validation, and sensitivity analyses, the reader is referred to the works of Andrews et al. [25] and Andriulli et al. [30].

Appendix B. Numerical Models

Appendix B.1. Fluid Code: OpenFOAM

The fluid model is run in the OpenFOAM [44] open source code. The starting conditions depend on the type of propellant and the simulated setup. The BCs follow the physical methodology, and as such use Neuman, Dirichlet, and Robin BCs. Table A1 reports the chosen time step and mesh cell size of the fluid simulation. In addition, Table A1 reports the numerical schemes with which derivatives in the equations of the physical model are linearized into a single matrix of equations for each variable or property along with the linear solvers and convergence algorithm used to solve said matrix. Appropriate source and sink terms, originating from the plasma chemistry and RF power deposition ensure that the mass flux is conserved.

Table A1. OpenFOAM simulation system settings.

Time and Mesh	
dt	1.00×10^{-11} s
min cell length	50 µm
max cell length	500 µm
Numerical Schemes	
time derivatives	backward 2nd order, implicit
gradients	Face limited, 2nd order, Gaussian integration + linear interpolation
divergence	Gauss interpolation with MUSCL interpolation
interpolation	linear
surface normal gradient	Explicit non-orthogonal correction
distance to wall	meshWave calculation
Matrix Solver	
phi	GAMG
pressures	GAMG
transonic pressures	PBiCGStab
electron densities	PBICGStab
neutral densities	PCG
ion density	PBiCGStab
velocities	PBiCGStab
algorithm	SIMPLE, 3 correctors, 1 outer corrector

Appendix B.2. Kinetic Code: Starfish

The kinetic model uses the PIC Starfish open-source code [45]. Starfish injects plasma particles at a source surface into an initially empty domain and continues to track them until convergence. The amount of injected particles is determined by the density, temperature, and drift velocity of the corresponding species. A minimum total macroparticle count of 700,000 per species was found to be a good compromise between limited computational time and reasonably low numerical noise (a count of 10–20 particles per cell is usually granted with this setup). As a result, the macroparticle weights for the plasma species ranged from 0.5×10^7 to 1.5×10^7. Throughout the simulation, the total amount of macroparticles in the domain did not vary more than 6%, and settled within 2% of the initial 700,000 per species at convergence. Thus, mass remained conserved throughout the kinetic simulation. The computational cost of the simulation was heavily dictated by the mesh size and time step. The spacing of the former should be smaller than the Debye length $\lambda_D = \sqrt{\epsilon_0 k_B T_e / n_e q^2}$, while the latter should be small enough to resolve the plasma frequency $\omega_{pe} = \sqrt{n_e q^2 / \epsilon_0 m_e}$. In order to reduce the computational load enforced by these stringent requirements, two numerical acceleration schemes were utilized [72]. First, the vacuum permittivity ϵ_0 was increased by a factor γ^2, which increases the Debye length λ_D by γ while reducing the plasma frequency by $1/\gamma$. This scaling allowed for a less fine mesh, making for fewer total macroparticles, as well as a larger time-step. Second, the mass of the heavy particles was reduced by a factor f, resulting in a velocity increase of $\sqrt{f}$. These schemes resulted in an approximate simulation time reduction of $\gamma^2\sqrt{f}$. Based on an earlier sensitivity analysis [25], the factors used in this work were $\gamma = 26.7$ and $f = 250$, respectively. These factors ensured that the thruster outlet, where the mesh is finest, could be resolved with 20 cells ($R_* = 20\lambda_D$). After the simulation concluded, the affected parameters were scaled back to their physical values during postprocessing. After approximately 25,000 iterations to reach convergence, the solution was averaged over an additional 50,000 iterations to minimize noise. The output included field values of the macroscopic plasma properties interpolated from the macroparticles at every mesh node. The model set the injection source surface, which coincides with the domain interface, at zero potential. Macroparticle motion, described in Equation (A12), was solved using the leapfrog Boris algorithm [73]. Collision processes were modeled through the Direct Simulation Monte Carlo (DSMC) and Monte Carlo Collision (MCC) methods, considering the following seven types of collision [25]:

1. Electron–electron Coulomb scattering [48]
2. Electron–ion Coulomb scattering [48]
3. Electron–neutral elastic scattering [74]
4. Ionization
5. Ion–neutral elastic scattering [75]
6. Ion–neutral charge exchange [76]
7. Neutral–neutral elastic scattering [77].

Neutral particle expansion was handled separately from charged particles in order to reduce runtime, with interactions between charged and neutral particles calculated by setting the neutral plume expansion solution as a background for modeling charged species.

References

1. Charles, C.; Boswell, R. Current-free double-layer formation in a high-density helicon discharge. *Appl. Phys. Lett.* **2003**, *82*, 1356–1358. [CrossRef]
2. Chen, F.F. Helicon discharges and sources: A review. *Plasma Sources Sci. Technol.* **2015**, *24*, 014001. [CrossRef]
3. Bellomo, N.; Manente, M.; Trezzolani, F.; Gloder, A.; Selmo, A.; Mantellato, R.; Toson, E.; Cappellini, L.; Duzzi, M.; Magarotto, M.; et al. Enhancement of microsatellites' mission capabilities: Integration of REGULUS electric propulsion module into UniSat-7. In Proceedings of the 70th International Astronautical Congress (IAC), Washington, DC, USA, 21–25 October 2019.
4. Jiménez, P.; Zhou, J.; Navarro-Cavallé, J.; Fajardo, P.; Merino, M.; Ahedo, E. Analysis of a cusped helicon plasma thruster discharge Analysis of a cusped helicon plasma thruster discharge. *Plasma Sources Sci. Technol.* **2023**, *32*, 18. [CrossRef]

5. Coppola, G.; Panelli, M.; Battista, F. Preliminary design of helicon plasma thruster by means of particle swarm optimization. *AIP Adv.* **2023**, *13*, 055209. [CrossRef]
6. Shumeiko, A.I.; Telekh, V.D. Direct thrust measurements of 2U-sized bi-directional wave plasma thruster. *AIP Adv.* **2023**, *13*, 085312. [CrossRef]
7. Wachs, B.N.; Jorns, B.A. *Optimization of an ECR Thruster using Single, Two Frequency, and Pulsed Waveforms*; American Institute of Aeronautics and Astronautics Inc., AIAA: Starbase, TX, USA, 2021. [CrossRef]
8. Désangles, V.; Packan, D.; Jarrige, J.; Peterschmitt, S.; Dietz, P.; Scharmann, S.; Holste, K.; Klar, P.J. ECRA thruster advances: 30W and 200W prototypes latest performances. *J. Electr. Propuls.* **2023**, *2*, 10. [CrossRef]
9. Magarotto, M.; Melazzi, D.; Pavarin, D. Study on the influence of the magnetic field geometry on the power deposition in a helicon plasma source. *J. Plasma Phys* **2019**, *85*, 905850404. [CrossRef]
10. Fruchtman, A. Electric Field in a Double Layer and the Imparted Momentum. *Phys. Rev. Lett.* **2006**, *96*, 065002. [CrossRef]
11. Fruchtman, A.; Takahashi, K.; Charles, C.; Boswell, R.W. A magnetic nozzle calculation of the force on a plasma. *Phys. Plasmas* **2012**, *19*, 033507. [CrossRef]
12. Manente, M.; Trezzolani, F.; Mantellato, R.; Scalzi, D.; Schiavon, A.; Souhair, N.; Duzzi, M.; Cappellini, L.; Barbato, A.; Paulon, D.; et al. REGULUS: Iodine Fed Plasma Propulsion System for Small Satellites. In Proceedings of the The 36th International Electric Propulsion Conference IEPC-2019-417, Vienna, Austria, 15–20 September 2019.
13. Bellomo, N.; Magarotto, M.; Manente, M.; Trezzolani, F.; Mantellato, R.; Cappellini, L.; Paulon, D.; Selmo, A.; Scalzi, D.; Minute, M.; et al. Design and In-orbit Demonstration of REGULUS, an Iodine electric propulsion system. *CEAS Space J.* **2022**, *14*, 79–90. [CrossRef]
14. Souhair, N.; Magarotto, M.; Andriulli, R.; Ponti, F. Prediction of the Propulsive Performance of an Atmosphere-Breathing Electric Propulsion System on Cathode-Less Plasma Thruster. *Aerospace* **2023**, *10*, 100. [CrossRef]
15. Dalle Fabbriche, S.; Souhair, N.; Magarotto, M.; Andriulli, R.; Corti, E.; Ponti, F. Development of a Global Model for the Analysis of Plasma in an Atmosphere-Breathing Cathode-Less Thruster. *Aerospace* **2023**, *10*, 389. [CrossRef]
16. Takahashi, K. Magnetic nozzle radiofrequency plasma thruster approaching twenty percent thruster efficiency. *Sci. Rep.* **2021**, *11*, 2768. [CrossRef] [PubMed]
17. Guaita, M.; Magarotto, M.; Manente, M.; Pavarin, D.; Lavagna, M. Semi-Analytical Model of a Helicon Plasma Thruster. *IEEE Trans. Plasma Sci.* **2022**, *50*, 425–438. [CrossRef]
18. Winglee, R.; Ziemba, T.; Giersch, L.; Prager, J.; Carscadden, J.; Roberson, B. Simulation and laboratory validation of magnetic nozzle effects for the high power helicon thruster. *Phys. Plasmas* **2007**, *14*, 063501. [CrossRef]
19. Lafleur, T. Helicon plasma thruster discharge model. *Phys. Plasmas* **2014**, *21*, 043507. [CrossRef]
20. Magarotto, M.; Melazzi, D.; Pavarin, D. 3D-VIRTUS: Equilibrium condition solver of radio-frequency magnetized plasma discharges for space applications. *Comput. Phys. Commun.* **2020**, *247*, 106953. [CrossRef]
21. Souhair, N.; Magarotto, M.; Majorana, E.; Ponti, F.; Pavarin, D. Development of a lumping methodology for the analysis of the excited states in plasma discharges operated with argon, neon, krypton, and xenon. *Phys. Plasmas* **2021**, *28*, 093504. [CrossRef]
22. Ahedo, E.; Navarro-Cavallé, J. Helicon thruster plasma modeling: Two-dimensional fluid-dynamics and propulsive performances. *Phys. Plasmas* **2013**, *20*, 043512. [CrossRef]
23. Choudhuri, A.R. *The Physics of Fluids and Plasmas*; Cambridge University Press: Cambridge, UK, 1998. [CrossRef]
24. Fede, S.D.; Manente, M.; Comunian, P.J.; Magarotto, M. Magnetic nozzle performance in a cluster of helicon plasma thrusters. *Plasma Sources Sci. Technol.* **2023**, *32*, 065013. [CrossRef]
25. Andrews, S.; Fede, S.D.; Magarotto, M. Fully kinetic model of plasma expansion in a magnetic nozzle. *Plasma Sources Sci. Technol.* **2022**, *31*, 035022. [CrossRef]
26. Sánchez-Villar, Á.; Zhou, J.; Ahedo, E.; Merino, M. Coupled plasma transport and electromagnetic wave simulation of an ECR thruster. *Plasma Sources Sci. Technol.* **2021**, *30*, 045005. [CrossRef]
27. Zhou, J.; Pérez-Grande, D.; Fajardo, P.; Ahedo, E. Numerical treatment of a magnetized electron fluid model within an electromagnetic plasma thruster simulation code. *Plasma Sources Sci. Technol.* **2019**, *28*, 115004. [CrossRef]
28. Magarotto, M.; Di Fede, S.; Souhair, N.; Andrews, S.; Ponti, F. Numerical suite for cathodeless plasma thrusters. *Acta Astronaut.* **2022**, *197*, 126–138. [CrossRef]
29. Andrews, S.; Andriulli, R.; Souhair, N.; Fede, S.D.; Pavarin, D.; Ponti, F.; Magarotto, M. Coupled global and PIC modelling of the REGULUS cathode-less plasma thrusters operating on xenon, iodine and krypton. *Acta Astronaut.* **2023**, *207*, 227–239. [CrossRef]
30. Andriulli, R.; Andrews, S.; Souhair, N.; Magarotto, M.; Ponti, F. Fully kinetic study of facility pressure effects on RF-source magnetic nozzles. *Acta Astronaut.* **2024**, *215*, 362–372. [CrossRef]
31. Souhair, N.; Ponti, F.; Magarotto, M.; Pavarin, D. Analysis of different numerical approaches for the simulation of a Helicon Plasma Thruster. In Proceedings of the 37th International Electric Propulsion Conference (IEPC), Boston, MA, USA, 19 June 2022.
32. Adamovich, I.; Baalrud, S.; Bogaerts, A.; Bruggeman, P.; Cappelli, M.; Colombo, V.; Czarnetzki, U.; Ebert, U.; Eden, J.G.; Favia, P.; et al. The 2017 Plasma Roadmap: Low temperature plasma science and technology. *J. Phys. D Appl. Phys.* **2017**, *50*, 323001. [CrossRef]
33. Adamovich, I.; Agarwal, S.; Ahedo, E.; Alves, L.L.; Baalrud, S.; Babaeva, N.; Bogaerts, A.; Bourdon, A.; Bruggeman, P.; Canal, C.; et al. The 2022 Plasma Roadmap: Low temperature plasma science and technology. *J. Phys. D Appl. Phys.* **2022**, *55*, 373001. [CrossRef]

34. Fiala, A.; Pitchford, L.C.; Boeuf, J.P. Two-dimensional, hybrid model of low-pressure glow discharges. *Phys. Rev. E* **1994**, *49*, 5607–5622. [CrossRef]
35. Bose, D.; Govindan, T.R.; Meyyappan, M. Modelling of magnetic field profile effects in a helicon source. *Plasma Sources Sci. Technol.* **2004**, *13*, 553–561. [CrossRef]
36. Chen, G.; Raja, L.L. Fluid modeling of electron heating in low-pressure, high-frequency capacitively coupled plasma discharges. *J. Appl. Phys.* **2004**, *96*, 6073–6081. [CrossRef]
37. Brown, D.L.; Walker, M.L.; Szabo, J.; Huang, W.; Foster, J.E. Recommended practice for use of faraday probes in electric propulsion testing. *J. Propuls. Power* **2017**, *33*, 582–613. [CrossRef]
38. Lobbia, R.B.; Beal, B.E. Recommended practice for use of langmuir probes in electric propulsion testing. *J. Propuls. Power* **2017**, *33*, 566–581. [CrossRef]
39. Bukowski, J.; Graves, D.; Vitello, P. Two-dimensional fluid model of an inductively coupled plasma with comparison to experimental spatial profiles. *J. Appl. Phys.* **1996**, *80*, 2614–2623. [CrossRef]
40. Souhair, N.; Magarotto, M.; Ponti, F.; Pavarin, D. Analysis of the plasma transport in numerical simulations of helicon plasma thrusters. *AIP Adv.* **2021**, *11*, 115016. [CrossRef]
41. Magarotto, M.; Manente, M.; Trezzolani, F.; Pavarin, D. Numerical Model of a Helicon Plasma Thruster. *IEEE Trans. Plasma Sci.* **2020**, *48*, 835–844. [CrossRef]
42. Fede, S.D.; Magarotto, M.; Andrews, S.; Pavarin, D. Simulation of the plume of a magnetically enhanced plasma thruster with SPIS. *J. Plasma Phys.* **2021**, *87*, 905870611. [CrossRef]
43. Souhair, N. Development of Numerical Tools for the Simulation, Design and Optimization of a Helicon Plasma Thruster. Dissertation Thesis, Università di Bologna, Bologna, Italy, 2023.
44. OpenFOAM. Available online: https://www.openfoam.com/ (accessed on 21 October 2024).
45. Brieda, L.; Keidar, M. Development of the starfish plasma simulation code and update on multiscale modeling of hall thrusters. In Proceedings of the 48th AIAA/ASME/SAE/ASEE Joint Propulsion Conference & Exhibit, Atlanta, GA, USA, 30 July–1 August 2012. [CrossRef]
46. Takahashi, K. Helicon-type radiofrequency plasma thrusters and magnetic plasma nozzles. *Rev. Mod. Plasma Phys.* **2019**, *3*, 1–61. [CrossRef]
47. Correyero, S.; Jarrige, J.; Packan, D.; Ahedo, E. Plasma beam characterization along the magnetic nozzle of an ECR thruster. *Plasma Sources Sci. Technol.* **2019**, *28*, 095004. [CrossRef]
48. Bittencourt, J.A. *Fundamentals of Plasma Physics*; Springer: New York, NY, USA, 2004. [CrossRef]
49. Ahedo, E.; Merino, M. Two-dimensional supersonic plasma acceleration in a magnetic nozzle. *Phys. Plasmas* **2010**, *17*, 73501. [CrossRef]
50. Ebersohn, F.; Raja, L.; Shebalin, J. Resistive Magnetohydrodynamic Study of Magnetic Field Effects on Plasma Plumes. In Proceedings of the 4th AIAA Plasmadynamics and Lasers Conference, San Diego, CA, USA, 24–27 June 2013. [CrossRef]
51. van Lynden, W.; Souhair, N.; Andriulli, R.; Magarotto, M.; Cervone, A.; Ponti, F. Novel Coupling Methods for Fluid and Kinetic Solvers in the numerical modeling of Helicon Plasma Thrusters. In Proceedings of the 74th International Astronautical Congress (IAC), Baku, Azerbaijan, 2–6 October 2023.
52. Manente, M.; Trezzolani, F.; Magarotto, M.; Fantino, E.; Selmo, A.; Bellomo, N.; Toson, E.; Pavarin, D. REGULUS: A propulsion platform to boost small satellite missions. *Acta Astronaut.* **2019**, *157*, 241–249. [CrossRef]
53. Trezzolani, F.; Magarotto, M.; Manente, M.; Pavarin, D. Development of a counterbalanced pendulum thrust stand for electric propulsion. *Measurement* **2018**, *122*, 494–501. [CrossRef]
54. Bellomo, N.; Magarotto, M.; Manente, M.; Trezzolani, F.; Mantellato, R.; Cappellini, L.; Paulon, D.; Selmo, A.; Scalzi, D.; Minute, M.; et al. REGULUS: Integration and Testing of an iodine Electric Propulsion System. In Proceedings of the Space Propulsion Conference, Estoril, Portugal, 17–19 March 2020.
55. Allan, M.; Zatsarinny, O.; Bartschat, K. Near-threshold absolute angle-differential cross sections for electron-impact excitation of argon and xenon. *Phys. Rev. A* **2006**, *74*, 030701. [CrossRef]
56. PHELPS Database. Available online: https://www.lxcat.net/Phelps (accessed on 1 January 2021).
57. Sommerer, T.J. Model of a weakly ionized, low-pressure xenon dc positive column discharge plasma. *J. Phys. D Appl. Phys.* **1996**, *29*, 769–778. [CrossRef]
58. BIAGI v7 Database. Available online: https://www.lxcat.net/Biagi-v7.1 (accessed on 1 January 2021).
59. Hyman, H.A. Electron-impact ionization cross sections for excited states of the rare gases (Ne, Ar, Kr, Xe), cadmium, and mercury. *Phys. Rev. A* **1979**, *20*, 855–859. [CrossRef]
60. COP Database. Available online: https://www.lxcat.net/COP (accessed on 1 January 2021).
61. Priti.; Gangwar, R.K.; Srivastava, R. Collisional-radiative model of xenon plasma with calculated electron-impact fine-structure excitation cross-sections. *Plasma Sources Sci. Technol.* **2019**, *28*, 025003. [CrossRef]
62. Vinci, A.E.; Mazouffre, S. Direct experimental comparison of krypton and xenon discharge properties in the magnetic nozzle of a helicon plasma source. *Phys. Plasmas* **2021**, *28*, 033504. [CrossRef]
63. Sudit, I.D.; Chen, F.F. Discharge equilibrium of a helicon plasma. *Plasma Sources Sci. Technol.* **1996**, *5*, 43. [CrossRef]
64. Siddiqui, M.U.; Cretel, C.; Synowiec, J.; Hsu, A.G.; Young, J.A.; Spektor, R. First performance measurements of the phase four RF thruster. In Proceedings of the 35th International Electric Propulsion Conference, Atlanta, GA, USA, 8–12 October 2017.

65. Magarotto, M.; Fede, S.D.; Souhair, N.; Andrews, S.; Manente, M.; Ponti, F.; Pavarin, D. Numerical Suite for Magnetically Enhanced Plasma Thrusters. In Proceedings of the 72 nd International Astronautical Congress, Dubai, United Arab Emirates, 25–29 October 2021.
66. Kushner, M.J. Modeling of magnetically enhanced capacitively coupled plasma sources: Ar discharges. *J. Appl. Phys.* **2003**, *94*, 1436–1447. [CrossRef]
67. Chen, F.F. *Introduction to Plasma Physics and Controlled Fusion*; Springer International Publishing: Berlin/Heidelberg, Germany, 2016. [CrossRef]
68. Lieberman, M.A.; Lichtenberg, A.J. *Principles of Plasma Discharges and Materials Processing*, 2nd ed.; Wiley-Interscience: Hoboken, NJ, USA, 2005; pp. 43–82.
69. Mikellides, I.G.; Katz, I.; Goebel, D.M.; Polk, J.E. Hollow cathode theory and experiment. II. A two-dimensional theoretical model of the emitter region. *J. Appl. Phys.* **2005**, *98*, 113303. [CrossRef]
70. Hagelaar, G.J.M.; de Hoog, F.J.; Kroesen, G.M.W. Boundary conditions in fluid models of gas discharges. *Phys. Rev. E* **2000**, *62*, 1452–1454. [CrossRef] [PubMed]
71. Gallina, G.; Magarotto, M.; Manente, M.; Pavarin, D. Enhanced biDimensional pIc: An electrostatic/magnetostatic particle-in-cell code for plasma based systems. *J. Plasma Phys.* **2019**, *85*, 905850205. [CrossRef]
72. Szabo, J.; Warner, N.; Martinez-Sanchez, M.; Batishchev, O. Full Particle-In-Cell Simulation Methodology for Axisymmetric Hall Effect Thrusters. *J. Propuls. Power* **2014**, *30*, 197–208. [CrossRef]
73. Qin, H.; Zhang, S.; Xiao, J.; Liu, J.; Sun, Y.; Tang, W.M. Why is Boris algorithm so good? *Phys. Plasmas* **2013**, *20*, 084503. [CrossRef]
74. Szabo, J.J. Fully Kinetic Numerical Modeling of a Plasma Thruster. Ph.D. Thesis, Massachusetts Institute of Technology, Cambridge, MA, USA, 2001.
75. Dalgarno, A.; McDowell, M.C.; Williams, A. The mobilities of ions in unlike gases. *Philos. Trans. R. Soc. Lond. Ser. A Math. Phys. Sci.* **1958**, *250*, 411–425.
76. Rapp, D.; Francis, W.E. Charge exchange between gaseous ions and atoms. *J. Chem. Phys.* **1962**, *37*, 2631–2645. [CrossRef]
77. Koura, K.; Matsumoto, H. Variable soft sphere molecular model for air species. *Phys. Fluids A Fluid Dyn.* **1992**, *4*, 1083–1085. [CrossRef]